This is a preprint, the final version is subject to change, of the American Mineralogist (MSA)
Cite as Authors (Year) Title. American Mineralogist, in press.
(DOI will not work until issue is live.) DOI: http://dx.doi.org/10.2138/am-2017-6186

Revision 1

Protoenstatite: A new mineral in Oregon sunstones with "watermelon" colors

Huifang Xu * [1], Tina R. Hill[1], Hiromi Konishi[1#], and Gabriela Farfan[2##]

[1] Department of Geoscience, University of Wisconsin-Madison, Madison, Wisconsin 53706, U.S.A.

[2] Madison West High School, 30 Ash Street, Madison, Wisconsin, 53726, U.S.A.

(Submitted to "*American Mineralogist*" as letter)

Present address: Department of Geology, Niigata University, Niigata 850-2181, Japan

Present address: MIT-WHOI Joint Program in Oceanography and Applied Ocean Science & Engineering, Woods Hole, MA 02543

*Corresponding author

hfxu@geology.wisc.edu

This is a preprint, the final version is subject to change, of the American Mineralogist (MSA)
Cite as Authors (Year) Title. American Mineralogist, in press.
(DOI will not work until issue is live.) DOI: http://dx.doi.org/10.2138/am-2017-6186

Abstract

Al-Fe-bearing protoentatite was discovered in Oregon sunstones with unusual pleochroic / dichroic red to green coloration using high-resolution transmission electron microscopy (HRTEM) and X-ray energy dispersive spectroscopy (EDS). The empirical formula calculated on the basis of 6 O *apfu* is $(Mg_{1.17}Fe_{0.43}Al_{0.26}Ca_{0.03}Na_{0.10}Ti_{0.01})_{\sum 2.00}(Si_{1.83}Al_{0.17})_{\sum 2.00}O_6$. The protoenstatite has a space group of *Pbcn*; its unit-cell parameters refined from selected-area electron diffraction patterns are a = 9.25(1) Å, b = 8.78(1) Å, and c = 5.32(1) Å. The esds on the cell parameters were determined based on electron diffraction patterns from the coexisting native copper inclusion and the host labradorite with known cell parameters. Protoenstatite nanocrystals are quenchable to low temperature. The crystallographically-oriented nanocrystals of protoenstatite and clinoenstatite in association with copper nanocrystals are responsible for the unusual green and "watermelon" coloration of the labradorite gemstone.

Keywords: Oregon sunstone, labradorite, new pyroxene, clinoenstatite, protoenstatite, HRTEM, native copper, dichroic

Introduction

Enstatite, $Mg_2Si_2O_6$, with a space group of *Pbca*, has several polymorphic counterparts including clinoenstatite ($P2_1/c$), high-temperature clinoenstatite (*C2/c*), high-pressure clinoenstatite (*C2/c*), protoenstatite (*Pbcn*), and high-pressure protoenstatite ($P2_1cn$) (Cameron and Papike 1981; Tribaudino et al., 2002; Angel et al., 1992; Yang et al., 1999). Protenstatite is reported to be a high temperature form that cannot be quenched to room temperature (Cameron and Papike 1981; Tribaudino et al., 2002). Protoenstatite would transform to enstatite or clinoenstatite at low temperature based on the results of synthetic protoenstatite (Cameron and Papike, 1981; Chen and Prensnall, 1975; Smith, 1969; Smyth, 1974). However, a synthetic Li-Sc-bearing protoenstatite with smaller cations of Li and Sc in octahedral sites is quenchable at low temperature (Smyth and Ito, 1975). It is reported that protoenstatite was a precursor of clinoenstatite in some Mg-rich basalts (Dallwitz et al., 1966; Shiraki et al., 1980) and even in star dusts (Schmitz and Brenker, 2008). In this letter, results from electron diffraction and high-resolution TEM (HRTEM) imaging are presented. The mineral and name have been approved by Commission on New Minerals, Nomenclature and Classification (CNMNC) of the International Mineralogical Association (IMA 2016-117). Two characterized specimens (catalogue numbers UWGM 3538 and UWGM 3539) are deposited in the collections of the Geology Museum, Department of Geoscience, University of Wisconsin-Madison (1215 West Dayton Street, Madison, WI 53706, USA).

Samples and Experimental Methods

Protoenstatite occurs as precipitates associated with copper nanocrystals in gem-quality labradorite phenocrysts (Oregon sunstones) from Dust Devil Mine, Lake County, Oregon

(Figures 1 and 2). The site is located in the Rabbit Basin within the Oregon high desert. The host rock is a mid-Miocene basalt (Johnson et al., 1991; Peterson, 1972). The phenocrysts are generally tabular plates and large laths ranging from ~1 cm in the greatest dimension to lathes 8.3 cm long, 2.6 cm wide and 1 cm thick (Hofmeister and Rossman, 1985; Johnson et al., 1991; Peterson, 1972; Stewart et al. 1966). Protoenstatite was discovered in the green part of the "watermelon" variety that possesses a clear rim and a core of transparent red surrounded by a clear vibrant green border that can only be seen in certain orientations (Figure 1). Some carved or faceted red, green and watermelon Oregon sunstones are illustrated in supplementary material (Fig. S1).

The "watermelon" sunstones exhibit pleochroism and dichroism. Color and schiller are always localized in the cores of the phenocrysts where the native copper micro- or nano-platelets that populate the interior are exsolved clusters of crystals. They are most commonly exsolved parallel to the feldspar crystal plane (010), but also (001) (Hofmeister and Rossman, 1985). This dichroism is exhibited in hand samples of "watermelon" sunstones. The crystals exhibit dichroism with a clear red when oriented approximately parallel to the feldspar (001) plane, and both red and green are seen when oriented in [100] and [010] directions (Figures 1). The parts with green color also exhibit a brownish red / green pleochroism under a plane polarized light (Figure 2). The same phenomenon was observed by Johnson et al. (1991). Pleochroism appears to become stronger in deeply colored specimens. By contrast, the clear rim does not show pleochroism.

Because protoenstatite occurs as nano-inclusions in gem-quality "watermelon" sunstones,

ion-milled TEM specimens (on Mo grids) were used for the mineralogical characterization using transmission electron microscope associated with an X-ray energy-dispersive spectroscopy (EDS) system. HRTEM imaging, X-ray EDS and selected-area electron diffraction (SAED) analyses were carried out using a Philips CM200-UT microscope equipped with GE light element energy-dispersive X-ray EDS at the Materials Science Center, University of Wisconsin-Madison, and operated at 200 kV. Chemical analyses were obtained using the EDS (spot size 5 with a beam diameter of ~50 nm). Quantitative EDS results were obtained using experimentally determined k-factors from standards of albite, forsterite, anorthite, orthoclase, labradorite, fayalite, and titanite. The same method was used for characterizing nanocrystals of luogufengite, Al-bearing ε-Fe_2O_3, (Xu et al., 2017).

Results and Discussion

TEM images show the protoenstatite nano-precipitates within labradorite together with native copper nanocrystals (Fig. 3). SAED patterns reveal their proto-pyroxene structure with the space group *Pbcn* (Fig. 4). X-ray EDS analysis confirms their pyroxene stoichiometry (Fig. 5, Table 1). The empirical formula calculated on the basis of 6 O *apfu* is $(Mg_{1.17}Fe_{0.43}Al_{0.26}Ca_{0.03}Na_{0.10}Ti_{0.01})_{\sum 2.00}(Si_{1.83}Al_{0.17})_{\sum 2.00}O_6$. HRTEM image shows (100) lattice fringes with a periodicity of 9.25 Å corresponding to periodic changes of skews of octahedral layers along the ***a***-axis (Fig. 6). The observed HRTEM image matches protoenstatite structure, instead of enstatite or clinoenstatite (See Table 2 for comparison).

Unit cell parameters were determined based on diffraction patterns from the protoenstatite nanocrystals. Neighbouring copper nanocrystals and the labradorite host were used as internal standards. Unit cell parameters of the labradorite with a very similar composition

(from Lake County, Oregon) are from Wenk et al. (1980). The measured unit-cell parameters are a = 9.25(1) Å, b = 8.78(1) Å, and c = 5.32(1) Å. Calculated density of protoenstatite is 3.30 $g \cdot cm^{-3}$. Calculated powder X-ray diffraction peaks are listed in Supplementary Material (Table S1). Comparison among the enstatite polymorphs with pyroxene structures is listed in table 2.

The crystals larger than ~ 200 nm transformed into clinoenstatite with a high density of stacking faults (Fig. S5), which is very similar to the observed microstructures in a fast-cooled protoenstatite (Ijima and Buseck, 1975). Cooling of the lava resulted in transformations from protoenstatite to clinoenstatite with a high density of stacking faults in large protoenstatite crystals (> 200 nm), whereas small protoenstatite crystals (< 200nm) are preserved in the host labradorite phenocrysts. The Al-bearing protoenstatite nanocrystals with large surface areas may lower the phase transformation temperature and stabilize the structure at low temperature. Similar phenomenon occurs in hematite-luogufengite system (Lee and Xu, 2016). It is also reported that protoenstatite nanocrystals with a large surface area of 615 m^2/g, synthesized using sol-gel and freeze-dry methods, can be quenched to room temperature (Jones et al, 1999). Protoenstatite nanocrystals were synthesized by sol-gel method at 800 °C (Jones et al, 1999), which is lower than the reported phase transition temperature (~1000 °C).

Implications

The labradorite (An_{65}) phenocrysts are very homogeneous in composition (Stewart et al., 1966; Wenk et al., 1980). We infer that the cores of "watermelon" crystals formed at early stages of magma chamber formation at high P-T conditions. The clear phenocryst rims without any precipitates suggest that they formed at a late stage under different conditions. Crystallization of protoenstatite and associated native copper might happen also at a late stage but before magma

131 eruption. The collective effect of the oriented crystals of protoenstatite and clinoenstatite results
132 in the vibrant green colour of "watermelon" sunstones. These results may help understand and
133 determine size-dependent stability of these minerals. We agree that the phenocrysts experienced
134 a thermal shock due to the rapid rising and quenching of the crystals (Hofmeister and Rossman
135 1985). This thermal shock origin can explain why the labradorite crystals without schiller and
136 colors are all cracked. The colored sunstones are thus thermal shock resistant. Like a "single
137 crystal concrete," their nano-inclusions of protoenstatite and Cu probably serve as cushion to
138 absorb the thermal shock due to metallic / plastic behavior of the Cu nanocrystals. This observed
139 texture may inspire the design of new crystalline materials that have strengths to resist thermal
140 shock while being optically clear and colorful.

141

142 **ACKNOWLEDGMENTS**

143 Authors thank Dr. Hongwu Xu and two anonymous reviewers for many constructive
144 suggestions and comments. This study was supported by NSF (EAR-0810150, EAR-1530614)
145 and the NASA Astrobiology Institute (N07-5489). Samples were collected by G. Farfan, C.
146 Peralta and the Dust Devil Mining Company.

147

148

149

REFERENCES

Angel, R.J., Chopelas, A., and Ross, N.L. (1992) Stability of high-pressure clinoenstatite at upper-mantle pressures. Nature, 358, 322-324.

Cameron, M., and Papike, J.J. (1981) Structural and chemical variations in pyroxenes. American Mineralogist, **66**, 1–50.

Chen, C.-H. and Presnall, D.C. (1975) The system Mg_2SiO_4-SiO_2 at pressure up to 25 kilobars. American Mineralogist, **60**, 398-406.

Dallwitz, W.B., Green, D. H., and Thompson, J. E. (1966) Clinoenstatite in a volcanic rock from the Cape Vogel area, Papua. Journal of Petrology, **7(3)**, 375-403.

Hofmeister, A. M., and Rossman, G. R. (1985) Exsolution of metallic copper from Lake County labradorite. Geology, **13(9)**, 644-647.

Ijima, S., and Buseck, P. R. (1975) High resolution electron microscopy of enatatite I: twinning, polymorphism, and polytypism. American Mineralogist, **60**, 758-770.

Johnston, C. L., Gunter, M. E., and Knowles, C. R. (1991). Sunstone Labradorite from the Ponderosa Mine, Oregon. Gems and Gemology, **XXVII**, 220-233.

Jones, S. A., Burlitch, J. M, Duchamp, J. C., and Duncan, T. M. (1999) Sol-gel synthesis of protoenstatite and a study of the factors that affect crystallization. Journal of Sol-Gel Science and Technology, 15, 201-209.

Lee, S., and Xu, H. (2016) Size-dependent phase map and phase transformation kinetics for nanometeric iron(III) oxides (g→e→a pathway). The Journal of Physical Chemistry C, 120, 13316–13322.

171 Murakami, T., Takeuchi, Y., and Yamanaka, T. (1982) The transition of orthoenstatite to
172 protoenstatite and the structure at 1080°C. Zeitschrift für Kristallographie, **160**, 299-312.

173 Peterson, N. (1972) Oregon "Sunstones". The Ore Bin, **34(12)**, 197-215.

174 Schmitz, S. and Brenker, F.B. (2008) Microstructural Indications for Protoenstatite Precursor of
175 Cometary $MgSiO_3$ Pyroxene: A Further High-Temperature Component of Comet Wild 2.
176 The Astrophysical Journal, 681 (2008) L105. doi:10.1086/590411.

177 Shiraki, K., Kuroda, N., Urano, H., and Maruyama, S. (1980) Clinoenstatite in boninites from the
178 Bonin Islands, Japan. Nature, **285**, 31-32.

179 Smith, J. V. (1969) Crystal structure and stability of $MgSiO_3$ polymorphs: physical properties
180 and phase relations of Mg-Fe pyroxenes. Mineralogical Society of America Special
181 Paper, **2**, 3–29.

182 Smyth, J. R. (1974) Experimental study on the polymorphism of enstatite. American
183 Mineralogist, **59**, 345-352.

184 Smyth, J.R. and Ito, J. (1975) The synthesis and crystal structure of a magnesium-lithium-
185 scandium protopyroxene. American Mineralogist, 62, 1252–1257.

186 Stewart, D., Walker, G., Wright, T., and Fahey, J. (1966) Physical Properties of Calcic
187 Labradorite from Lake County, Oregon. American Mineralogist, **51**, 177-197.

188 Tribaudino, M., Nestola, F., Camara, F., and Domeneghetti, M. C. (2002) The high-temperature
189 $P2_1/c$-$C2/c$ phase transition in Fe-free pyroxene ($Ca_{0.15}Mg_{1.85}Si_2O_6$): Structural and
190 thermodynamic behavior. American Mineralogist, Volume 87, pages 648–657.

191 Wenk, H. R., Joswig, W., Tagai, T., Korekawa, M., and Smith, B. K. (1980) The average
192 structure of An 62-66 labradorite. American Mineralogist, **65**, 81-95.
193 Xu, H.F., Lee, S., and Xu, H.W. (2017) Luogufengite: a new nano-mineral of Fe_2O_3 polymorph
194 with giant coercive field. American Mineralogist, **102**, 711-719.
195 Yang, H. Finger, L.W., Conrad, P.G., Prewitt, C.T., and Hazen, R.M. (1999) A new pyroxene
196 structure at high pressure: Single-crystal X-ray and Raman study of the Pbcn-$P2_1cn$ phase
197 transition in protopyroxene. American Mineralogist, **84**, 245–256.

198
199

This is a preprint, the final version is subject to change, of the American Mineralogist (MSA)
Cite as Authors (Year) Title. American Mineralogist, in press.
(DOI will not work until issue is live.) DOI: http://dx.doi.org/10.2138/am-2017-6186

Figures and Captions

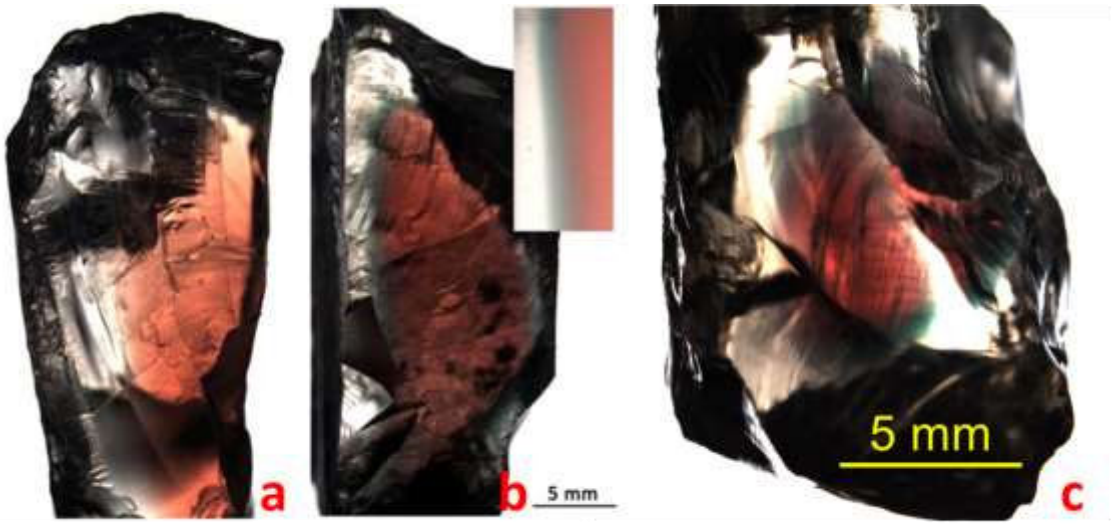

Figure 1. A gem-quality “watermelon" Oregon sunstone looked down along the normal of (001) (a), and along ***b***-axis (b). Note the exceptionally clear rim, along with the zoning of colors. The green border becomes brownish red when looked down along the normal of (001) (a). Top up-right inset shows the detail of the red to green transition from a polished sample (~ 4 mm thick) (b). Dark areas are due to uneven surfaces that bend the transmitted light away. Another “watermelon” sunstone (c) with a clear rim looked down along ~***b***-axis under a transmitted light from bottom (left). Linear features with dark color in red core and green board are microplates of native Cu.

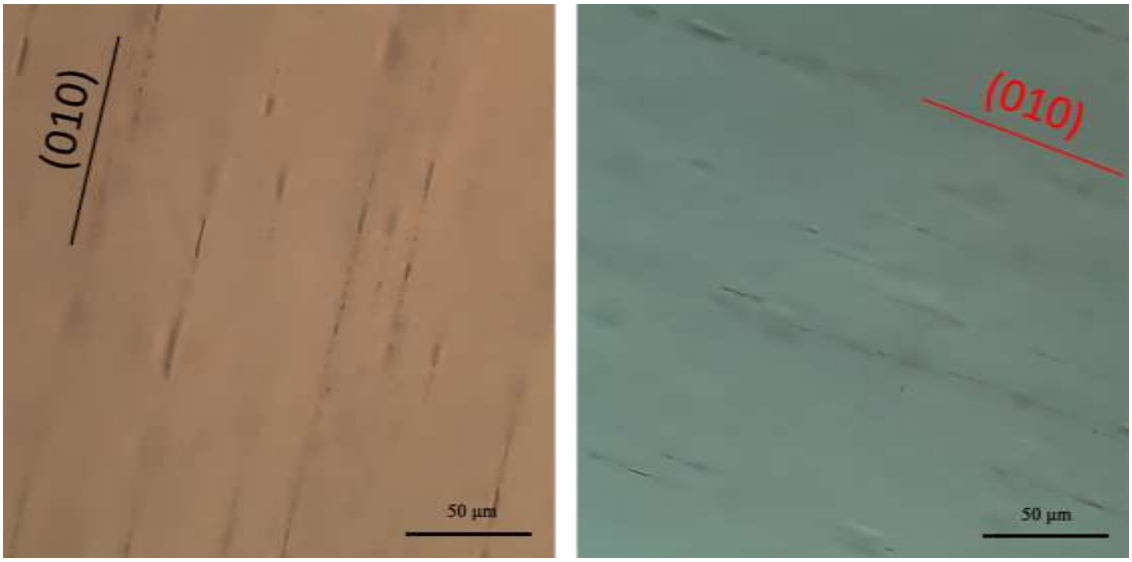

Figure 2: Transmitted light photomicrographs of a polished sunstone crystal (~ 5 mm thickness) from the green border part show pleochroism (light brown to pale green). The cleavage plane (001) is perpendicular to the light. Some inclusions appear as linear features distributed along the (010) plane of labradorite. The appearance of the inclusions is much larger than their actual sizes due to the strain existing between thenanocrystals and the host labradorite.

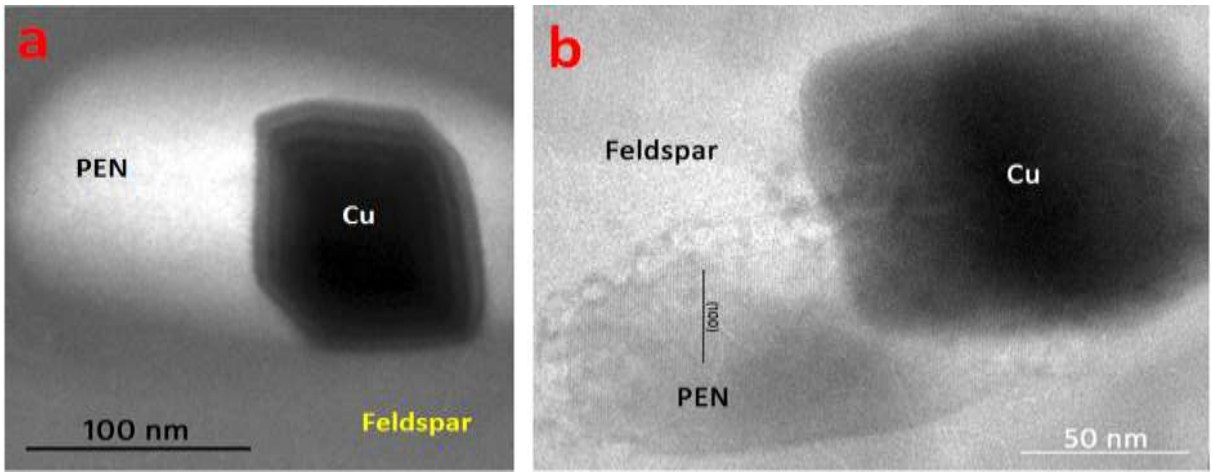

Figure 3. Dark-field TEM image (a) and bright-field TEM image (b) showing two protoenstatite (PEN) nanocrystals together with native copper nanocrystals (Cu) within labradorite.

This is a preprint, the final version is subject to change, of the American Mineralogist (MSA)
Cite as Authors (Year) Title. American Mineralogist, in press.
(DOI will not work until issue is live.) DOI: http://dx.doi.org/10.2138/am-2017-6186

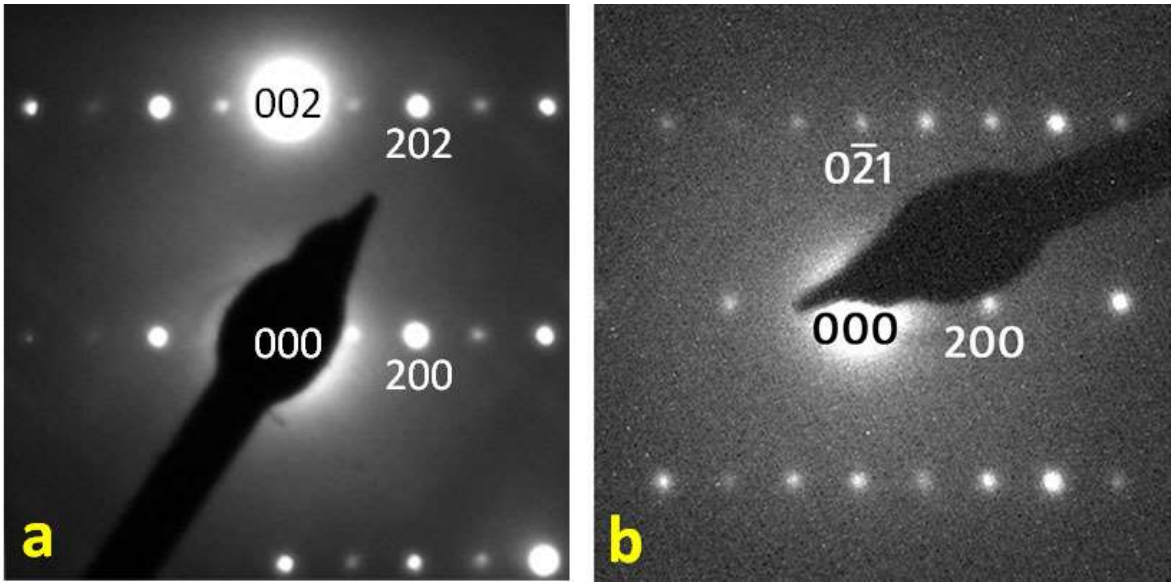

Figure 4. SAED patterns of protoenstatite nanocrystals shown in Figure 1 along ~ [010] zone-axis (a) and along [012] zone-axis (b). The very strong 002 diffraction spot in the SAED pattern (a) is due to very small excitation error (or diffraction error) for 200, which means that the crystal is very close to two-beam condition. Weak *h*00 (*h* = 2*n*+1) reflections that violate the 2-fold screw axis symmetry result from multiple diffraction that is common in electron diffraction, especially from thick specimens. The *h*00 (*h* = 2*n*+1) reflections are extinct from a smaller and thinner crystal (b). The multiple diffraction effect is not obvious here. The SAED patterns confirm the *Pbcn* symmetry.

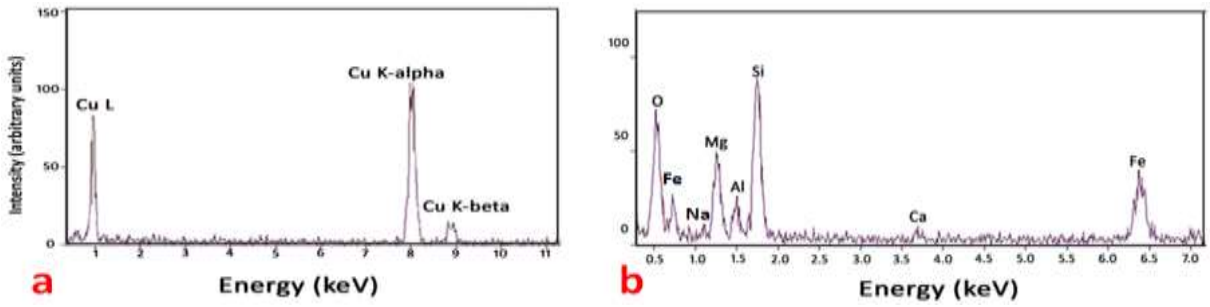

Figure 5. X-ray EDS spectra from a copper nanocrystal (a) and a protoenstatite nano-crystal (b).

This is a preprint, the final version is subject to change, of the American Mineralogist (MSA)
Cite as Authors (Year) Title. American Mineralogist, in press.
(DOI will not work until issue is live.) DOI: http://dx.doi.org/10.2138/am-2017-6186

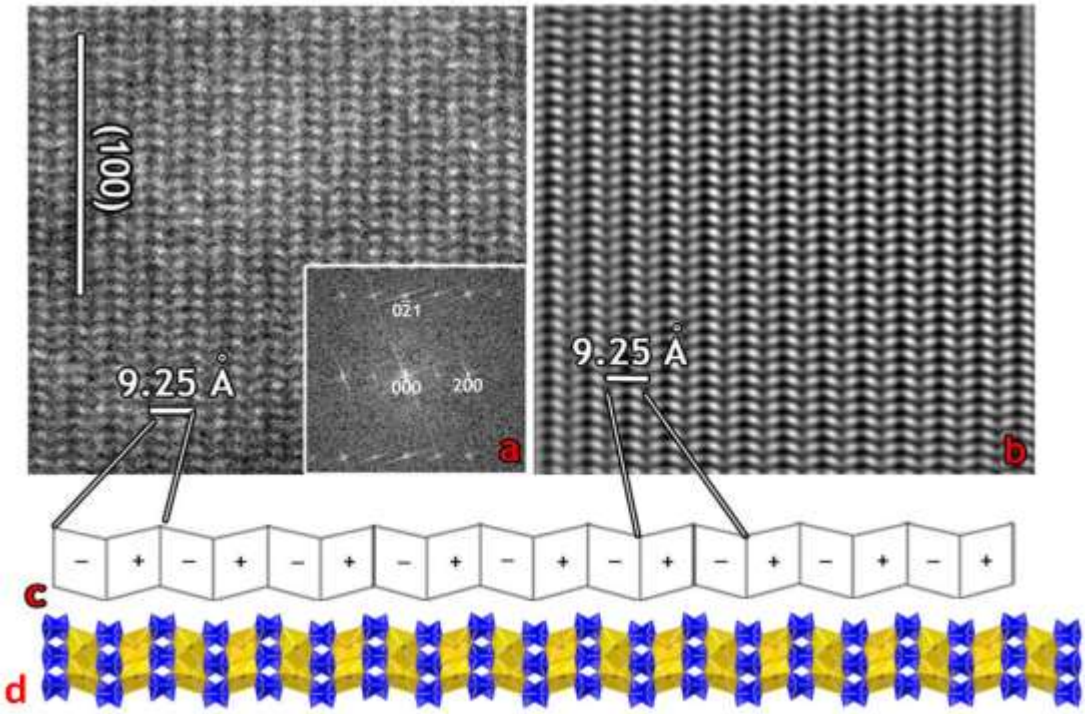

Figure 6. HRTEM image (a) and noise-filtered HRTEM image (b) of a protoenstatite nanocrystal showing (100) lattice fringes with a periodicity of 9.25 Å. A [012] zone-axis fast Fourier transform (FFT) pattern is inserted at the lower-right corner of the HRTEM image. (c) A simple protoenstatite model based on unit-cell twining of clinoenstatite. (d) A polyhedral model of protoenstatite projected onto (010) showing periodic changes of skews of octahedral layers along the ***a***-axis. The model is based on a Li-Sc-bearing protoenstatite at room temperature (Yang et al., 1999) with unit cell parameters and composition measured from the protoenstatite nanocrystals.

This is a preprint, the final version is subject to change, of the American Mineralogist (MSA)
Cite as Authors (Year) Title. American Mineralogist, in press.
(DOI will not work until issue is live.) DOI: http://dx.doi.org/10.2138/am-2017-6186

Table.1 Chemical compositions of protoenstatite.

	(1)	(2)	(3)	Average
SiO_2	49.73	51.41	51.60	50.91
TiO_2	0.74	0.37	0.37	0.50
Al_2O_3	11.23	10.23	9.14	10.20
FeO	13.71	15.05	14.05	14.27
MgO	22.57	20.82	22.51	21.97
CaO	0.78	0.73	1.02	0.84
Na_2O	1.24	1.41	1.44	1.37
Si^T	1.78	1.85	1.85	1.82
Ti	0.02	0.01	0.01	0.01
Al^{M1}	0.25	0.28	0.23	0.25
Al^T	0.22	0.15	0.16	0.18
Fe	0.41	0.45	0.42	0.43
Mg	1.20	1.11	1.20	1.17
Ca	0.03	0.03	0.04	0.03
Na	0.09	0.10	0.10	0.09

Table 2: Comparison among all enstatite polymorphs

Phase	Space group	Chain rotation	Skew of octahedra	β angle (°)
Enstatite (En)*	*Pbca*	OA, OB	+ + - - + + - -	90
Clinoenstatite (CEN)*	$P2_1/c$	SA, OB	+ + + +	~ 108
High-CEN**	*C2/c*	O	+ + + +	~ 109
High-P CEN***	*C2/c*	O	+ + + +	~ 101
Protoenstatite (PEN)*	*Pbcn*	O	+ - + -	90
High-P PEN****	$P2_1cn$	SA, OB	+ - + -	90

Notes: * Cameron and Papike 1981; ** Tribaudino et al. (2002); *** Angel et al. (1992); **** Yang et al. (1999).